

THE HUBBLE SPACE TELESCOPE WIDE FIELD CAMERA 3 EARLY RELEASE SCIENCE DATA: PANCHROMATIC FAINT OBJECT COUNTS FOR 0.2–2 μm WAVELENGTH*

ROGIER A. WINDHORST¹, SETH H. COHEN¹, NIMISH P. HATHI², PATRICK J. MCCARTHY³, RUSSELL E. RYAN, JR.⁴, HAOJING YAN⁵,
 IVAN K. BALDRY⁶, SIMON P. DRIVER⁷, JAY A. FROGEL⁸, DAVID T. HILL⁷, LEE S. KELVIN⁷, ANTON M. KOEKEMOER⁹,
 MATT MECHTLEY¹, ROBERT W. O’CONNELL¹⁰, AARON S. G. ROBOTHAM⁷, MICHAEL J. RUTKOWSKI¹, MARK SEIBERT³,
 AMBER N. STRAUGHN¹¹, RICHARD J. TUFFS¹², BRUCE BALICK¹³, HOWARD E. BOND⁹, HOWARD BUSHOUSE⁹, DANIELA CALZETTI¹⁴,
 MARK CROCKETT¹⁵, MICHAEL J. DISNEY¹⁶, MICHAEL A. DOPITA¹⁷, DONALD N. B. HALL¹⁸, JON A. HOLTZMAN¹⁹,
 SUGATA KAVIRAJ¹⁵, RANDY A. KIMBLE¹¹, JOHN W. MACKENTY⁹, MAX MUTCHLER⁹, FRANCESCO PARESCE²⁰, ABIHIT SAHA²¹,
 JOSEPH I. SILK¹⁴, JOHN T. TRAUGER²², ALISTAIR R. WALKER²³, BRADLEY C. WHITMORE⁹, AND ERICK T. YOUNG²⁴

¹ School of Earth and Space Exploration, Arizona State University, P.O. Box 871404, Tempe, AZ 85287-1404, USA; Rogier.Windhorst@asu.edu

² Department of Physics & Astronomy, University of California, Riverside, CA 92521, USA

³ Observatories of the Carnegie Institution of Washington, Pasadena, CA 91101-1292, USA

⁴ Department of Physics, University of California, One Shields Avenue, Davis, CA 95616, USA

⁵ Center for Cosmology and AstroParticle Physics, The Ohio State University, Columbus, OH 43210, USA

⁶ Astrophysics Research Institute, Liverpool John Moores University, Birkenhead CH41 1LD, UK

⁷ School of Physics and Astronomy, University of St Andrews, Fife KY16 9SS, UK

⁸ Association of Universities for Research in Astronomy, Washington, DC 20005, USA

⁹ Space Telescope Science Institute, Baltimore, MD 21218, USA

¹⁰ Department of Astronomy, University of Virginia, Charlottesville, VA 22904-4325, USA

¹¹ NASA-Goddard Space Flight Center, Greenbelt, MD 20771, USA

¹² Max Planck Institute for Nuclear Physics (MPIK), Saupfercheckweg 1, D-69117 Heidelberg, Germany

¹³ Department of Astronomy, University of Washington, Seattle, WA 98195-1580, USA

¹⁴ Department of Astronomy, University of Massachusetts, Amherst, MA 01003, USA

¹⁵ Department of Physics, University of Oxford, Oxford OX1 3PU, UK

¹⁶ School of Physics and Astronomy, Cardiff University, Cardiff CF24 3AA, UK

¹⁷ Research School of Astronomy & Astrophysics, The Australian National University, Weston Creek, ACT 2611, Australia

¹⁸ Institute for Astronomy, University of Hawaii, Honolulu, HI 96822, USA

¹⁹ Department of Astronomy, New Mexico State University, Las Cruces, NM 88003, USA

²⁰ INAF–IASF Bologna, Via Gobetti 101, 40129 Bologna, Italy

²¹ National Optical Astronomy Observatories, Tucson, AZ 85726-6732, USA

²² NASA-Jet Propulsion Laboratory, Pasadena, CA 91109, USA

²³ Cerro Tololo Inter-American Observatory, La Serena, Chile

²⁴ NASA-Ames Research Center, Moffett Field, CA 94035, USA

Received 2010 June 7; accepted 2011 January 27; published 2011 March 21

ABSTRACT

We describe the *Hubble Space Telescope* (*HST*) Wide Field Camera 3 (WFC3) Early Release Science (ERS) observations in the Great Observatories Origins Deep Survey (GOODS) South field. The new WFC3 ERS data provide calibrated, drizzled mosaics in the UV filters F225W, F275W, and F336W, as well as in the near-IR filters F098M (Y_s), F125W (J), and F160W (H) with 1–2 *HST* orbits per filter. Together with the existing *HST* Advanced Camera for Surveys (ACS) GOODS-South mosaics in the $BViZ$ filters, these panchromatic 10-band ERS data cover 40–50 arcmin² at 0.2–1.7 μm in wavelength at 0′.07–0′.15 FWHM resolution and 0′.090 Multidrizzled pixels to depths of $AB \simeq 26.0$ –27.0 mag (5σ) for point sources, and $AB \simeq 25.5$ –26.5 mag for compact galaxies. In this paper, we describe (1) the scientific rationale, and the data taking plus reduction procedures of the panchromatic 10-band ERS mosaics, (2) the procedure of generating object catalogs across the 10 different ERS filters, and the specific star–galaxy separation techniques used, and (3) the reliability and completeness of the object catalogs from the WFC3 ERS mosaics. The excellent 0′.07–0′.15 FWHM resolution of *HST*/WFC3 and ACS makes star–galaxy separation straightforward over a factor of 10 in wavelength to $AB \simeq 25$ –26 mag from the UV to the near-IR, respectively. Our main results are: (1) proper motion of faint ERS stars is detected over 6 years at 3.06 ± 0.66 mas year^{−1} (4.6σ), consistent with Galactic structure models; (2) both the Galactic star counts and the galaxy counts show mild but significant trends of decreasing count slopes from the mid-UV to the near-IR over a factor of 10 in wavelength; (3) combining the 10-band ERS counts with the panchromatic Galaxy and Mass Assembly survey counts at the bright end ($10 \text{ mag} \lesssim AB \lesssim 20 \text{ mag}$) and the Hubble Ultra Deep Field counts in the $BViZY_sJH$ filters at the faint end ($24 \text{ mag} \lesssim AB \lesssim 30 \text{ mag}$) yields galaxy counts that are well measured over the entire flux range $10 \text{ mag} \lesssim AB \lesssim 30 \text{ mag}$ for 0.2–2 μm in wavelength; (4) simple luminosity+density evolution models can fit the galaxy counts over this entire flux range. However, no single model can explain the counts over this entire flux range in all 10 filters *simultaneously*. More sophisticated models of galaxy assembly are needed to reproduce the overall constraints provided by the current panchromatic galaxy counts for $10 \text{ mag} \lesssim AB \lesssim 30 \text{ mag}$ over a factor of 10 in wavelength.

Key words: Galaxy: stellar content – infrared: galaxies – instrumentation: high angular resolution – ultraviolet: galaxies

Online-only material: color figures

1. INTRODUCTION

The study of the formation and evolution of galaxies and large-scale structure are amongst the most active interfaces between theory and observation in modern astrophysics. Galaxies are believed to have formed gradually over cosmic time from a combination of gas infall and mergers (Hopkins et al. 2006), regulated by feedback from stellar winds, supernovae (SNe), and/or active galactic nuclei (AGNs; e.g., Scannapieco et al. 2005; di Matteo et al. 2005). The origin of the Hubble sequence is not yet fully understood (e.g., Driver et al. 1998) but is likely related to the balance between major mergers versus minor accretion events and steady infall (e.g., Conselice et al. 2003; Hopkins et al. 2010; Peng et al. 2010). The critical epoch for the assembly of massive galaxies appears to be the ~ 4 Gyr span from redshift $z \simeq 3$ to $z \simeq 1$, where also the cosmic star formation history seems to have peaked (Madau et al. 1998; Hopkins 2004; Hopkins & Beacom 2006).

At redshifts $z \gtrsim 3$, deep *Hubble Space Telescope* (HST) imaging surveys and ground-based spectroscopy have revealed a paucity of massive galaxies and few classical disks or spheroids (e.g., Law et al. 2007, 2009). In contrast, large ground-based spectroscopic surveys targeting redshifts $z \lesssim 1$ —coupled with HST imaging—have shown that by this epoch massive galaxies are largely mature, and that the Hubble sequence has been mostly established (e.g., Abraham et al. 1996, 1999, 2007; Driver et al. 1995, 1998; Glazebrook et al. 1995; Lilly et al. 1998). While substantial growth ($\sim 50\%$) in the stellar mass of all galaxy types—including spheroids—may have occurred during the last ~ 7 Gyr, the process of major galaxy assembly was well underway by $z \simeq 1$ (e.g., de Lucia et al. 2006; Dickinson et al. 2003). The interim period—from redshifts of $z \simeq 3$ to $z \simeq 1$ —is the era in which much of the stellar mass in galaxies is accumulated (e.g., Dickinson et al. 2003; Abraham et al. 2007), and when galaxies acquire the characteristic structural and dynamical properties that define them today. The HST Wide Field Camera 3 (WFC3) was optimized to study this critical period of galaxy assembly.

WFC3 was successfully installed into HST on 2009 May 14, by the astronauts on board Space Shuttle Atlantis during the Space Transportation System mission 125 (STS-125). This shuttle mission was the fifth Servicing Mission of HST, however, for historical reasons, it is referred to as SM4. Many of the current co-authors were members of the WFC3 Science Oversight Committee (SOC) from 1998 July through 2009 November. Our main role as the SOC was to define the WFC3 science requirements and goals, monitor them during the pre-launch phases of the project, and to oversee the design, implementation, integration, and testing (both ground-based and on-orbit) of the WFC3 instrument.

The WFC3 provides a unique opportunity to compare the galaxy populations in the local and distant universe. With its wide spectral coverage ($0.2\text{--}1.7\ \mu\text{m}$), very high spatial resolution ($0''.04$ FWHM at $0.2\ \mu\text{m}$ to $0''.16$ FWHM at $1.6\ \mu\text{m}$), fine pixel sampling ($0''.039\ \text{pixel}^{-1}$ in the UVIS channel and $0''.13\ \text{pixel}^{-1}$ in the IR channel), and high sensitivity ($AB \simeq 26\text{--}27$ mag in two orbits; 5σ for point sources), many new interesting questions and outstanding problems can be addressed with the WFC3 data. By sampling the vacuum UV with high sensitivity and the very high angular resolution afforded by the

diffraction limited $2.4\ \text{m}$ *Hubble Space Telescope*, WFC3 can observe star-forming regions in galaxies over most of the Hubble time. The near-IR channel on WFC3 allows one to do rest-frame visible-band photometry of distant galaxies to low luminosities and over areas large enough to provide representative samples. Together, the panchromatic images produced by WFC3 allow the user to decompose distant galaxies into their constituent substructures, examine their internal stellar populations, and help constrain their dust content. In this Early Release Science (ERS) program, the UVIS and IR channels of WFC3 are used to provide a small, but representative sampling of the capabilities of WFC3 to examine the formation and evolution of galaxies in the critical galaxy assembly epoch of $z \simeq 1\text{--}3$, when the universe was only $6\text{--}2$ Gyr old, respectively.

Details of the HST WFC3 ERS program (PID 11359; PI: R. O’Connell) can be found on the Web.²⁵ The current ERS program was specifically conceived to make maximum use of these WFC3 capabilities, and to make an optimal comparison between the intermediate- and high-redshift galaxy samples identified in the current ERS program and nearby galaxies imaged in other HST programs. These capabilities were important WFC3 science drivers, while the instrument was designed and constructed from 1998 to 2008.

In the year that the intermediate-redshift WFC3 ERS data have been available, a number of papers have appeared or submitted that use this panchromatic data set. For instance, Ryan et al. (2011) discuss the evolution of passive galaxies using the WFC3 ERS observations and make a detailed study of their size evolution over cosmic time. Rutkowski et al. (2011) present a panchromatic catalog of early-type galaxies at intermediate redshifts ($z \simeq 0.3\text{--}1.5$) from the WFC3 ERS data and derive their rest-frame (FUV–V) and (NUV–V) colors as a function of redshift. Cohen et al. (2011) present a 10-band photometric study of distant galaxies in the WFC3 ERS data, measure reliable photometric redshifts, and derive their physical properties with cosmic time. Hathi et al. (2010) discuss UV-dropout galaxies in the Great Observatories Origins Deep Survey (GOODS)-South at redshifts $z \simeq 1.5\text{--}3$ from the WFC3 ERS data, and summarize the evolution of the faint-end luminosity function (LF) slope α and characteristic luminosity L^* from $z \simeq 8$ to $z \simeq 0$. Oesch et al. (2010b) similarly discuss the evolution of the ultraviolet LF from $z \sim 0.75$ to $z \sim 2.5$. Straughn et al. (2011) study faint emission-line galaxies from the WFC3 ERS IR grism observations. Van Dokkum & Brammer (2010) discuss WFC3 grism spectra and images of one growing compact galaxy at $z \simeq 1.9$. Finkelstein et al. (2011) discuss spatially resolved imaging of Ly α emission line objects at $z \simeq 4.4$ through parallel ACS F658N narrow-band images to the WFC3 ERS data, and their constraints as to how Lyman continuum photons escape from such objects.

Labbé et al. (2010) discuss the star formation rates and stellar masses of $z \simeq 7\text{--}8$ galaxies from IRAC observations of the WFC3/IR ERS and Hubble Ultra Deep Fields (HUDFs). Robertson (2010) estimates how to best improve the LF constraints from high-redshift galaxy surveys using WFC3 ERS data and from additional deep WFC3 survey data yet to be obtained. Bouwens et al. (2010a) discuss potentially very blue UV-continuum slopes of low luminosity galaxies at $z \simeq 7$ from the WFC3 ERS IR data, and their possible implications for very low metallicities in these objects. Bouwens et al. (2010b) also discuss $z \simeq 8$ galaxy candidates seen in the ultradeep WFC3/IR

* Based on observations made with the NASA/ESA *Hubble Space Telescope*, which is operated by the Association of Universities for Research in Astronomy, Inc., under NASA contract NAS 5-26555.

²⁵ <http://www.stsci.edu/cgi-bin/get-proposal-info?11359>

observations of the HUDF. Yan et al. (2011a) probe the bright end of the galaxy LF at $z \gtrsim 7$ using *HST* pure parallel observations, and discuss these in context of the WFC IR observations in the ERS and in the HUDF. Yan et al. (2011b) discuss galaxy formation in the reionization epoch from the WFC3 observations of the HUDF, and suggest an LF at $z \simeq 8$ –10 that differs from that found by Bouwens et al. (2010b) and Oesch et al. (2010a). Wyithe et al. (2011) explain that part of this discrepancy may arise due to distortion of the very high redshift galaxy number counts through gravitational lensing by random foreground galaxies at $z \simeq 1$ –2. This boosts the number of $z \gtrsim 8$ –10 objects that become observable in the WFC3 IR samples, a non-negligible fraction of which therefore must be sought close to foreground galaxies at $z \simeq 1$ –2. These many examples show the great potential of the WFC3 ERS data presented in the current paper, and we refer the reader to these other papers for in-depth studies of the ERS data that are beyond the scope of the current paper. It suffices to say that the quality of and the scientific results from the ERS data exceeded the expectations of the WFC3 SOC, even though we have been involved with the WFC3 instrument from its conception in 1998.

In Section 2 of this paper, we present the WFC3 ERS survey strategy, the filters used and their achieved depths. In Section 3, we present the observations in both the WFC3 UVIS and IR channels, and the pointings and their areal coverage. In Section 4, we present the WFC3 data reduction procedures, their reliability and completeness, and their current limitations. In Section 5, we present the object finding procedures and catalog generation, and the star–galaxy separation procedure used and its reliability in the 10 ERS filters. In Section 6, we present the panchromatic ERS star counts and discuss the faint ERS stellar proper motion results. In Section 7, we present the panchromatic ERS galaxy counts from 0.2 – $1.7 \mu\text{m}$ to $\text{AB} \simeq 26$ – 27 mag, and compare these to the 10-band ground-based Galaxy and Mass Assembly (GAMA) survey counts for $10 \text{ mag} \lesssim \text{AB} \lesssim 20 \text{ mag}$ at the bright end, and to the HUDF counts in the *BVizY_sJH* filters (defined in Section 2.1) for $24 \text{ mag} \lesssim \text{AB} \lesssim 30 \text{ mag}$ at the faint end. We also present the panchromatic ERS images for interesting individual objects. In Section 8, we summarize our main results and conclusions. Throughout this paper, we use *Wilkinson Microwave Anisotropy Probe* (WMAP) year 7 cosmology (Komatsu et al. 2011), or $H_0 = 71 \text{ km s}^{-1} \text{ Mpc}^{-1}$, $\Omega_0 = 0.26$, and $\Lambda = 0.74$, and the AB_v magnitude system (Oke 1974).

2. WFC3 AND ITS CAPABILITIES

2.1. The ERS Filter Set

In the current ERS program, the unique panchromatic capabilities of WFC3 are used to survey the structure and evolution of galaxies at the peak of the galaxy assembly epoch at $z \simeq 1$ –3. Deep ultraviolet and near-IR imaging, and slitless near-IR spectroscopy of existing deep multi-color GOODS-S/ACS fields are used to gauge star formation and the growth of stellar mass as a function of galaxy morphology, structure and surrounding density in this critical cosmic epoch at redshifts $1 \lesssim z \lesssim 3$.

The total *HST* filter set provided by the WFC3 ERS imaging of the GOODS-South field is shown in Figure 1(a), and its properties are summarized in Tables 1 and 2. WFC3 adds the F225W, F275W, and F336W filters in the WFC3 UVIS channel, and the F098M, F125W, and F160W filters (hereafter *Y_sJH*) in the WFC3 IR channel. Together with the existing GOODS ACS F435W, F606W, F775W, and F850LP images (Giavalisco

et al. 2004), the new WFC3 UVIS and IR filters provide a total of 10 *HST* filters that span the wavelength range $\lambda \simeq 0.2$ – $1.7 \mu\text{m}$ nearly contiguously. We refer to this entire 10-band survey hereafter as the “ERS,” to these 10 filters as the “ERS filters,” and to the seven reddest ERS filters as the “*BVizY_sJH*” filters throughout. Details of the GOODS survey can be found in Giavalisco et al. (2004) and references therein. The top panel of Figure 1(a) compares the ERS filters to the spectral energy distribution (SED) of two single burst model galaxies (middle and bottom panels of Figure 1(a)) with ages of 0.1 and 1 Gyr at redshifts of $z = 0, 2, 4, 6$, and 8, respectively.

The ERS images in the WFC3 UVIS filters F225W, F275W, and F336W are used to identify galaxies at redshifts $z \gtrsim 1.5$ from their UV continuum breaks, which between the F225W and F275W filters is sampled at redshifts as low as $z \simeq 1.5$ – 1.7 (see Figure 1). These filters provide star formation indicators tied directly to both local and $z \gtrsim 3$ galaxy populations, which are the ones best observed through their Lyman breaks from the ground at $\lambda \gtrsim 350 \text{ nm}$. The critical new data that the WFC3 UVIS channel can provide are thus very high resolution, deep images for $0.2 \mu\text{m} \lesssim \lambda \lesssim 0.36 \mu\text{m}$, as illustrated in Figure 1(a).

The ERS images in the WFC3 near-IR filters F098M, F125W, and F160W are used to probe the Balmer and 4000 Å breaks and stellar mass function well below $10^9 M_\odot$ for mass-complete samples in the critical redshift range of $z \simeq 1$ –3. The unique new data that the WFC3 IR channel can provide are high-resolution, very sensitive near-IR photometry over fields larger than those possible with *HST* NICMOS, or over wide fields with adaptive optics from the ground (e.g., Steinbring et al. 2004; Melbourne et al. 2005).

2.2. ERS Grisms

In addition to these broadband ERS filters, we used the WFC3 near-IR grisms G102 and G141 to obtain slitless spectroscopy of hundreds of faint galaxies at a spectral resolution of $R \simeq 210$ – 130 , respectively. The WFC3 near-IR grism data can trace the primary indicators of star formation—the Ly α and H α emission-lines—in principle over the redshift range for $z \simeq 5$ – 13 and $z \simeq 0.2$ – 1.7 , respectively. WFC3 can also trace the Lyman break and the rest-frame UV continuum slope, as well as the Balmer and 4000 Å breaks over the redshift range $z \simeq 1$ – 9 and $z \simeq 0$ – 2.5 , respectively. The ERS grism program thus at least covers the peak of the cosmic star formation history at redshifts $1 \lesssim z \lesssim 2$, using some of the most important star formation and post-starburst indicators, while also providing some metallicity-independent reddening indicators. Both IR grism dispersers provide capabilities that cannot be reproduced from the ground: slitless spectroscopy of very faint objects ($\text{AB} \simeq 25$ – 26 mag) over a contiguous wide spectral range in the near-IR, that is not affected by atmospheric night-sky lines. The ERS grism observations are two orbits in depth each, covering a single WFC3 field, which was also covered in a previous ACS G800L grism survey (Straughn et al. 2009). An example of the ERS G141 and G102 grism spectra is shown in the figures of Appendix B.2. Further details of the ERS grism data reduction and the analysis of the faint emission line galaxies are given in Appendix B.2 and by Straughn et al. (2011).

WFC3 UVIS G280 UV-prism observations were not made as part of the 104 orbit intermediate-redshift ERS program, because of its much lower throughput and the significant overlap of its many spectral orders (Bond & Kim Quijano 2007; Wong et al. 2010). Currently, one Cycle 17 GO program (11594; PI: J. O’Meara) is using the WFC3 G280 prism to carry out

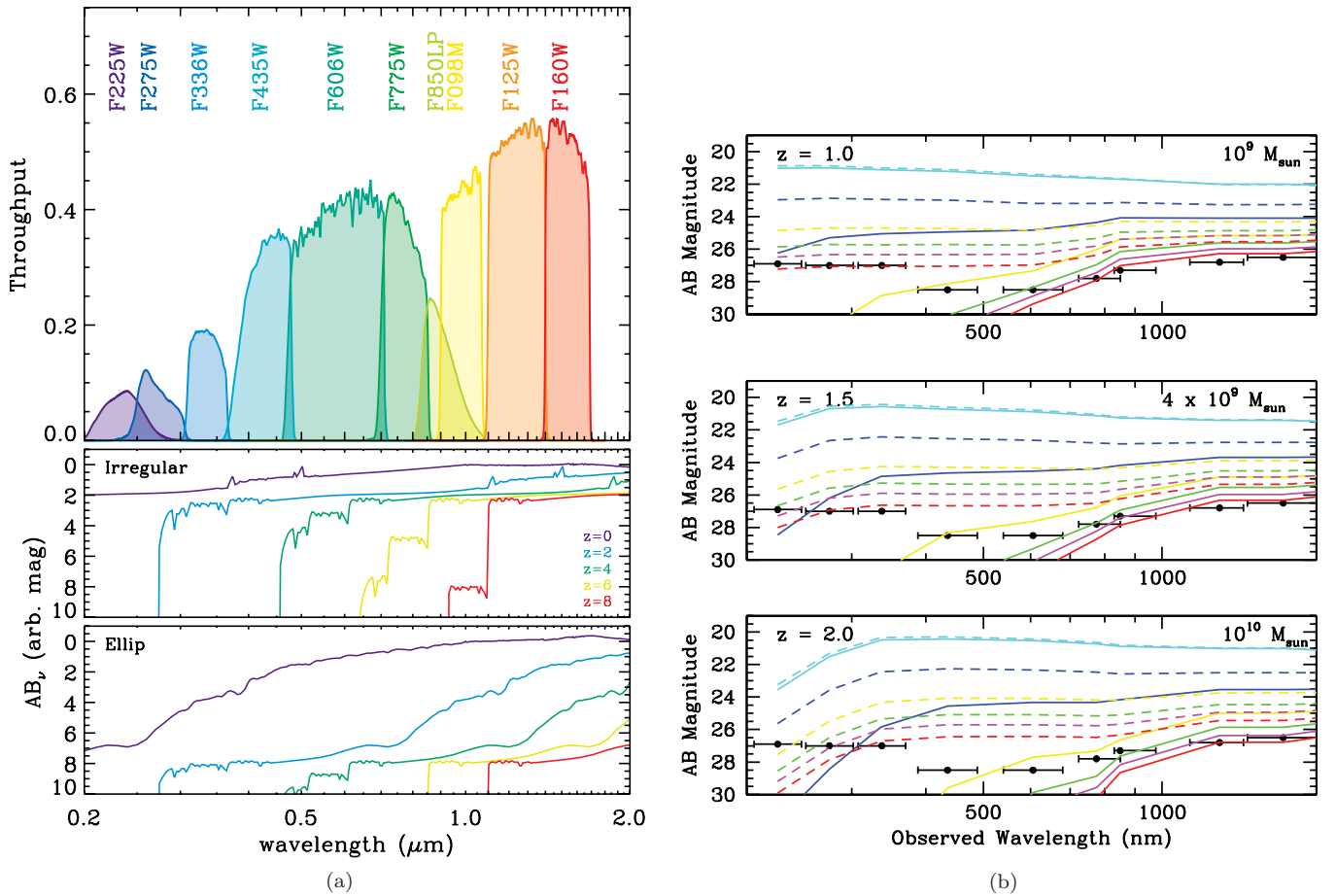


Figure 1. (a) Top panel: the full panchromatic *HST*/WFC3 and ACS filter set used in the ERS imaging of the GOODS-South field. Plotted is the overall system throughput, or the *HST* Optical Telescope Assembly throughput $\text{OTA} \times \text{filter transmission } T \times \text{detector QE}$. Middle and bottom panels: spectral energy distributions for two single burst model galaxies with ages of 0.1 and 1 Gyr and redshifts of $z = 0, 2, 4, 6$, and 8 are shown as black, blue, green, yellow, and red curves, respectively. Intergalactic medium absorption shortward of $\text{Ly}\alpha$ was applied following Haardt & Madau (1996). The UVIS filters sample the $\text{Ly}\alpha$ forest and Lyman continuum breaks, while the near-IR filters probe the 4000 Å and Balmer breaks at these redshifts. Additional photometry is available from ground-based VLT *K*-band imaging, and *Spitzer*/IRAC imaging at 3.5, 4.5, 5.6 and 8.5 μm. (b) Mass sensitivity of the WFC3 ERS filters used. The three panels show the depth of the WFC3 ERS images as horizontal bars, compared to evolving galaxy models of different masses at three redshifts. The top panel is for $z = 1$ and a stellar mass of $10^9 M_{\odot}$. The solid lines represent nearly instantaneous bursts, and the dashed lines are for declining star formation with a 1 Gyr e-folding time. The colors refer to ages of 10, 100, 500, 1000, 1400, 2000, and 3000 Myr from cyan to red. The middle panel shows similar models at $z = 1.5$ for $4 \times 10^9 M_{\odot}$, while the bottom panel is for $z = 2$ and masses of $10^{10} M_{\odot}$. At $z = 1$, the WFC3 ERS reaches masses of $0.02 M^*$ for typical star formation histories. Both the flux scale and the wavelength scale are logarithmic, illustrating WFC3's exquisite panchromatic coverage and sensitivity in probing the stellar masses of galaxies through its IR channel, and the star formation in galaxies through its UVIS channel.

(A color version of this figure is available in the online journal.)

a spectroscopic survey of Lyman limit absorbers at redshifts $1.8 \lesssim z \lesssim 2.5$. Readers interested in the WFC3 G280 prism performance should follow the results from that program.

2.3. ERS UVIS Filter Red-leaks and IR Filter Blue-leaks

In the context of the WFC UVIS and IR channel performance for intermediate- to high-redshift early- and late-type galaxies, it is useful to briefly summarize here the possible effects of UVIS channel filter red-leaks and IR channel filter blue-leaks on the measured fluxes of these objects. UVIS red-leaks are defined as the fraction of flux longward of 400 nm of an SED of given effective temperature T_{eff} that makes it erroneously into the UV filter. The IR blue-leaks are defined as the fraction of flux shortward of 830 nm of an SED of given effective temperature T_{eff} that makes it erroneously into the IR filter or grism (for details, see Wong et al. 2010).

The WFC3 UVIS filters were designed with great attention to minimize their red-leaks, which were much larger in the earlier generation WFPC2 UV filters. Similarly, the WFC3 IR filters

and grisms were designed to minimize the blue-leaks. For both sets of WFC3 filters, lower out-of-band transmission usually goes at the expense of lower in-band transmission, and vice versa. Hence, both the WFC3 and IR filters were designed and fabricated such that the in-band transmission was optimized as much as possible, while keeping the out-of-band transmission to acceptable or correctable levels for all SEDs expected in the relevant astrophysical situations.

The resulting WFC3 UVIS red-leaks are acceptably small ($\lesssim 10\%$) for all zero-redshift SEDs with $T_{\text{eff}} \gtrsim 5000$ K for the F225W filter, $T_{\text{eff}} \gtrsim 4000$ K for the F275W filter, and $T_{\text{eff}} \gtrsim 2000$ K for the F336W filter, respectively (Wong et al. 2010). For cooler ($T_{\text{eff}} \lesssim 2000\text{--}5000$ K) zero-redshift SEDs, some red-leak correction thus has to be applied to the observed F336W, F275, and F225W fluxes, respectively. However, for objects at substantial redshifts ($z \gtrsim 0.75\text{--}1$), the SED will shift out of the UVIS sensitivity regime quickly enough to significantly reduce the red-leak. Hence, the WFC3 UVIS red-leaks in general only need to be corrected for the reddest ($T_{\text{eff}} \lesssim 5000$ K), lower-

Table 1
Filters, Exposure Times, and Depths of the WFC3 ERS and GOODS-South ACS Data

Channel	Filter1	Filter2	Filter3	Filter4	Grism	Grism	Total Orbits
WFC3/UVIS	F225W	F275W	F336W		...		
Orbits	2	2	1		...		$5 \times 8 = 40$ Direct
Depth (AB)	26.3	26.4	26.1		...		
nJy	110	100	132		...		
ACS/WFC	F435W	F606W	F775W	F850LP	G800L		
Orbits	3	3	4	9	80		$15 \times 19 = 285$ Direct
Depth (AB)	27.9	28.1	27.5	27.3	27.0		$2 \times 20 = 40$ Grism
nJy	14	14	27	44	58		
WFC3/IR	F098M	F125W	F160W		G102	G141	
Orbits	2	2	2		2	2	$6 \times 10 = 60$ Direct
Depth (AB)	27.2	27.55	27.25		25.2	25.5	$1 \times 4 = 4$ Grism
nJy	48	36	48		303	230	
Total WFC3 ERS Orbits					(2009 Aug–2009 Oct)		104
Total ACS GOODS Orbits inside ERS					(2002 Jul–2005 Mar)		325
Total <i>HST</i> Orbits					(2002 Jul–2009 Oct)		429

Notes. Note 1: the orbital integration times listed are those as achieved for the WFC3 UVIS and IR ERS observations, as well as for the GOODS ACS v2.0 observations. For the ACS grism, 40 out of 200 orbits ACS G800L observations from the *HST* Cycle 14 PEARS project 10530 (PI: S. Malhotra; Malhotra et al. 2005; Pirzkal et al. 2004, 2005, 2009; Straughn et al. 2008, 2009) that reside inside the ERS mosaic are listed (see Figure 3). Note 2: the listed depth is the 50% completeness limit for 5σ detections in total SExtractor AB magnitudes for typical compact objects at this flux level (circular aperture with $0''.4$ radius; 0.50 arcsec² aperture), as derived from Figure 9. Note 3: for spectral continuum detection in the G102 and G141 grisms, these flux limits are about 2.0–1.8 mag brighter, respectively. Note 4: we note that the pre-flight WFC3 ETC sensitivity values were 0.15–0.2 mag more conservative in both the UVIS and the IR than the in-flight values quoted here in Table 1, as also shown in Figure 2. Note 5: due to the limited observing time available, and its poorer prism performance, UV-prism observations in P280 were not taken as part of the ERS.

Table 2
ERS Filters, PSFs, Zero Points, Sky Background, and Effective Area

<i>HST</i> - Instrument/ Mode	ERS Filter	Central Lambda (μm)	Filter FWHM (μm)	PSF FWHM ($''$)	Zero Point (AB mag@ $1\text{ e}^- \text{ s}^{-1}$)	Sky Background magarcsec ⁻²	Effective Area (arcmin ²)
WFC3/UVIS	F225W	0.2341	0.0547	0.092	24.06	25.46	53.2
WFC3/UVIS	F275W	0.2715	0.0481	0.087	24.14	25.64	55.3
WFC3/UVIS	F336W	0.3361	0.0554	0.080	24.64	24.82	51.6
ACS/WFC	F435W	0.4297	0.1038	0.080	25.673	23.66	72.4
ACS/WFC	F606W	0.5907	0.2342	0.074	26.486	22.86	79.2
ACS/WFC	F775W	0.7764	0.1528	0.077	25.654	22.64	79.3
ACS/WFC	F850LP	0.9445	0.1229	0.088	24.862	22.58	80.3
WFC3/IR	F098M	0.9829	0.1695	0.129	25.68	22.61	44.8
WFC3/IR	F125W	1.2459	0.3015	0.136	26.25	22.53	44.7
WFC3/IR	F160W	1.5405	0.2879	0.150	25.96	22.30	44.7

Notes. Note 1: the panchromatic PSF FWHM was measured from ERS stars as in Figures 7(a) and (b), and includes the contribution from the OTA and its wavefront errors, the specific instrument pixel sampling or Modulation Transfer Function (MTF). Note 2: the WFC3 zero points are in AB magnitudes for $1.0\text{ e}^- \text{ s}^{-1}$, taken from http://www.stsci.edu/hst/wfc3/phot_zp_lbn. Note 3: the GOODS *B*V_z sky-background values are from Hathi et al. (2008). Note 4: the effective areas used in this paper are in units of arcminutes squared for the effective number of WFC3 or ACS tiles available and used. Note 5: the GOODS v2.0 *B*V_z data release is from http://archive.stsci.edu/pub/hlsp/goods/v2/h_goods_v2.0_rdm.html. Note 6: the panchromatic effective ERS area was derived from Figures 8(a)–(c) for the WFC3 mosaics and the relevant GOODS tiles, and indicates the total area over which at least half of the total ERS exposure time was available. (Figure 8 shows that $\gtrsim 80\%$ of the total ERS exposure time was available for 50 arcmin^2 in the WFC3 UVIS filters, and for 40 arcmin^2 in the WFC3 IR filters.)

redshift ($z \lesssim 0.75$) SEDs observed in the bluest UVIS filters (F225W). Further details are given in Rutkowski et al. (2011).

The WFC3 IR blue-leaks are very small ($\lesssim 0.01\%$) for all zero-redshift SEDs with $T_{\text{eff}} \lesssim 10,000\text{ K}$ for the F098M, F105W, F125W, and F160W filters, and remains very small ($\lesssim 0.1\%$) even for the bluest zero-redshift SEDs with $T_{\text{eff}} \simeq 30,000\text{--}50,000\text{ K}$ (Wong et al. 2010). For higher-redshift SEDs ($z \gtrsim 1$) of any T_{eff} , the redshift further reduces the IR blue-leak. Similarly, the G141 grism was made on a glass substrate with no transmission below 750 nm , and is well blocked by its coatings

shortward of 1050 nm and long-ward of 1700 nm (Baggett et al. 2007). Hence, it also has acceptably a small blue-leak. The same is true for the higher-resolution G102 grism.

2.4. WFC3 Detectors and Achieved ERS Sensitivities

The WFC3 UV-blue optimized CCDs were chosen specifically to complement those of ACS. They were made by E2V in the UK, and are thinned, backside illuminated, CCD detectors with $2\text{ k} \times 4\text{ k}$ $15\text{ }\mu\text{m}$ ($0''.0395$) pixels, covering the

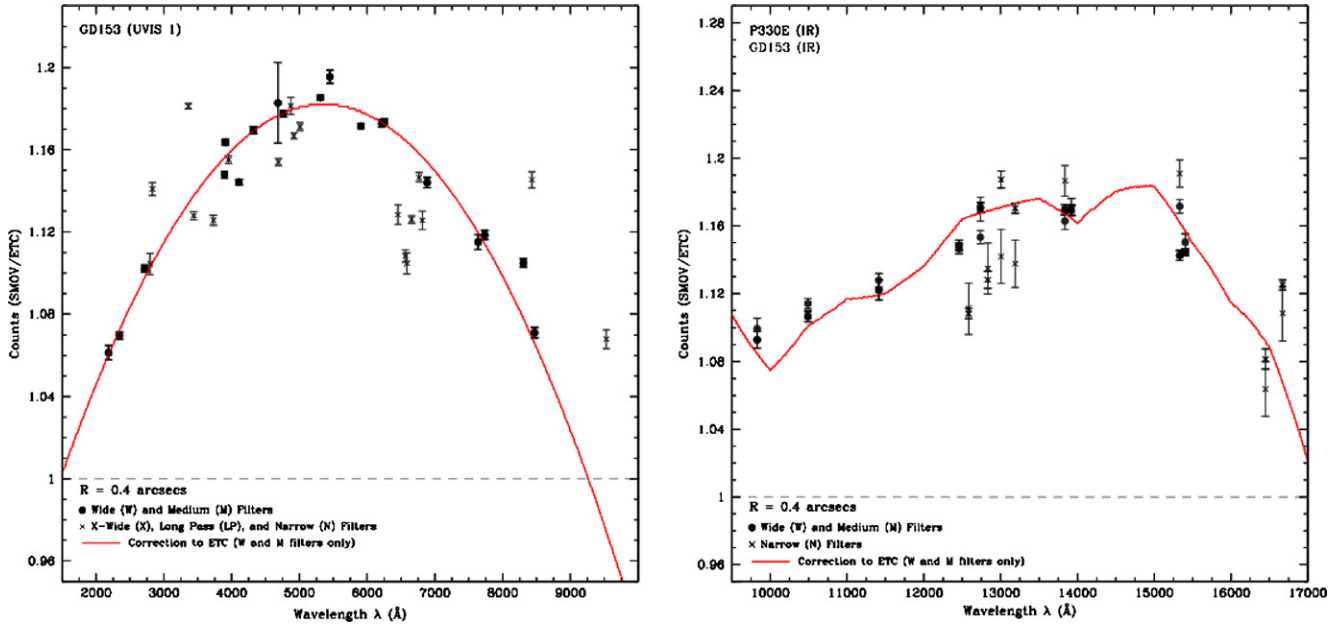


Figure 2. Ratio of on-orbit count rate to that obtained in ground-based thermal vacuum tests for various WFC3 filters in the UVIS (left panel) and IR (right panel), respectively. On-orbit rates are significantly higher than in ground tests. See the text for details.

(A color version of this figure is available in the online journal.)

wavelength range 200–1000 nm with Quantum Efficiency $QE \gtrsim 50\%$ throughout (Wong et al. 2010; Kimble et al. 2010). The total WFC3 UVIS field of view with these two CCDs is $162'' \times 162''$.

The WFC3 near-IR detectors were Teledyne HgCdTe infrared detectors (molecular beam epitaxy-grown and substrate removed) with Si CMOS Hawaii-1R multiplexers and have $1k \times 1k$ $18\mu m$ ($0''.130$) pixels, covering the wavelength range 800–1730 nm with $QE \gtrsim 77\%$ throughout (Wong et al. 2010; Kimble et al. 2010). The total WFC3 IR field of view is $123'' \times 136''$. Further specifications of the WFC3 detectors are listed where relevant below.

Table 1 summarizes the resulting WFC3 sensitivities from our relatively short ERS exposures. The table lists the number of orbits per filter and the 5σ depths in AB magnitudes and F_v units. A net exposure time of 2600–2700 s was available in each *HST* orbit for on-source ERS observations. In Figure 1(b), the equivalent depths are plotted in physical terms, by comparing with the spectral synthesis models of Bruzual & Charlot (2003) at the three fiducial redshifts, following Ryan et al. (2007, 2008, 2011). Simple stellar populations models with single bursts or exponentially declining star formation rates with an e-folding time of 1 Gyr are plotted. Figure 1(b) shows the predicted SEDs for models with ages ranging from 10 Myr to 3 Gyr, along with the 5σ depths of the WFC3 ERS program. The three panels represent redshifts $z = 1.0, 1.5$, and 2.0 , and models with stellar masses of $M = 10^9$, 4×10^9 , and $10^{10} M_\odot$, respectively. These SED tracks illustrate the intended SED and mass sensitivity of the WFC3 ERS observations as a function of cosmic epoch. Galaxies with ongoing star formation, even with fairly large ages, are easily detected in the WFC3 UV observations. At $z \simeq 2$, a maximally old $\tau \simeq 1$ model with a mass of $\sim 0.3 M^*$ is detectable above the WFC3 detection threshold in the F336W filter, while at $z \simeq 1$, the WFC3 ERS can detect young star-forming galaxies with masses as low as a few $\times 10^7 M_\odot$, or about a $M \sim 0.01 M^*$ galaxy in that filter.

Table 2 summarizes the *HST* instrument modes and the ERS filters used, the filter central wavelength λ , its width,

and the point-spread function (PSF) FWHM as a function of wavelength, the AB magnitude zero points for all 10 filters for a count rate of $1.0 e^- s^{-1}$, as well as the zodiacal sky background values in each ERS filter. The GOODS sky-background values in the F435W, F606W, F775W, and F850LP filters (hereafter *BViz*) are from Hathi et al. (2008).

Figure 2 shows that on average, the on-orbit WFC3 UVIS sensitivity is 6%–18% higher than the predicted pre-launch sensitivity from the ground-based thermal vacuum test (left panel), and the on-orbit WFC3 IR sensitivity is 9%–18% higher (right panel). The red lines are best fits to the in-flight/pre-launch sensitivity ratio. For the UVIS data, this is just a parabolic fit, as the in-flight/pre-launch excess does not seem to follow the CCD sensitivity curve (Kalirai et al. 2009a). For the IR data, a polynomial fit was folded with the IR detector sensitivity curve, since the in-flight/pre-launch does somewhat resemble the IR detector sensitivity curve (Kalirai et al. 2009b). The true cause of this beneficial, but significant discrepancy is unknown. It possibly results from uncertainties in the absolute calibration procedure of the optical stimulus used in the thermal vacuum tests of WFC3 (Kimble et al. 2010), and/or perhaps from slow temporal changes in the *HST* Optical Telescope Assembly (OTA) itself (Kalirai et al. 2009a, 2009b). The cause of this discrepancy is currently being investigated, and lessons learned will be applied to the upcoming ground-based calibrations of the *James Webb Space Telescope* (JWST) thermal vacuum absolute throughput measurements.

3. THE ERS DATA COLLECTION STRATEGY

The GOODS-South field was chosen for the ERS pointings, because of the large body of existing and publicly available data. Besides the deep, four-color ACS *BViz* imaging (Giavalisco et al. 2004; Dickinson et al. 2004), there are low-resolution ($R \sim 100$) ACS slitless G800L grism spectra covering the wavelength range ~ 0.55 – $0.95 \mu m$ (cf. Pirzkal et al. 2004; Malhotra et al. 2005; Ferreras et al. 2009; Rhoads et al. 2009; Straughn et al.

2008, 2009). There is also a wealth of ground- and space-based data, such as deep $U+R$ -band VLT/VIMOS imaging (Nonino et al. 2009), deep VLT/ISAAC JHK_s -band imaging (Retzlaff et al. 2010), a very large number of Very Large Telescope (VLT) spectra (Vanzella et al. 2005, 2009; Popesso et al. 2009; Balestra et al. 2010), deep *Chandra* X-ray images (Giacconi et al. 2002; 2 Msec by Luo et al. 2010; 4Msec by Luo et al. 2011), deep *XMM* X-ray observations (4 Msec by Comastri et al. 2011), *GALEX* UV data (Burgarella et al. 2006), *Spitzer* photometry with IRAC and MIPS (Papovich et al. 2005; Yan et al. 2004, 2005), *Herschel* FIR images at 70, 110, and 160 μm (Gruppioni et al. 2010; Lutz et al. 2011), and deep ATCA and Very Large Array radio images (cf. Afonso et al. 2006; Kellermann et al. 2008), respectively.

Given the constraint on the total amount of time available in the allotted 104 *HST* orbits, the ERS program could survey *one* 4×2 WFC3 mosaic covering $10' \times 5'$ or roughly 50 arcmin^2 to 5σ depths of $AB \simeq 26.0$ mag in the three bluest wide-band UVIS filters, and *one* 5×2 WFC3 mosaic covering $10' \times 4'$ or roughly 40 arcmin^2 to 5σ depths of $AB \simeq 27.0$ mag in the three near-IR filters. This angular coverage probes comoving scales of roughly 5–10 Mpc and provides a sample of 2000–7000 galaxies to $AB \simeq 26$ –27 mag in the panchromatic ERS images. The IR images were dithered to maximally match the UVIS field of view.

Figure 3 shows the ACS z' -band (F850LP) mosaic of the entire GOODS-South field, and the outline of the acquired WFC3 pointings, as well as the locations of the ACS images taken in parallel to the WFC3 ERS pointings. The ACS parallels were taken with the ACS/WFC filters F814W and F658N to search for high-redshift Ly α emitters at $z = 4.415 \pm 0.03$, of which several were known spectroscopically in the GOODS-South field (Vanzella et al. 2005; Finkelstein et al. 2011). The WFC3 ERS mosaic pointings cover the Northern $\sim 30\%$ of the GOODS-South field (Figure 3). The eight ERS pointings are contiguous with a tiling that can be easily extended to the South in future WFC3 GO programs (see, e.g., the Faber, Ferguson et al. Multi Cycle Treasury *HST* programs 12060–12064).

The orbital F225W and F275W ERS observations were designed to minimize possible Earth limb contamination. To guarantee the lowest possible UV sky background in the WFC3 images, one 1200 s F275W and one 1200 s F225W exposure was obtained in each orbit. All F225W exposures were taken at the end of each orbit, in contrast with the common practice of observing all exposures in the same filter in rapid succession in subsequent orbits. All three 800 s F336W exposures were obtained during the same single orbit for a given ERS pointing. This manner of scheduling indeed minimized the on-orbit UV sky background away from the Earth's limb (see Table 2), but it somewhat complicated the subsequent MultiDrizzle procedure (see Section 4.2), since no “same-orbit” cosmic ray rejection could be applied to the F225W and F275W images in order to find a first slate of bright objects for image alignment. Further details on the image alignment are given in Section 4 and Appendix A.

In the WFC3 IR channel, six exposures of 800–900 s were taken in each of the F098M, F125W, and F160W filters, using two orbits for each filter, but staying away from the Earth's limb at the end of each orbit in order to keep the near-IR sky background as low as possible (see Table 2). In total, 9 or 10 Fowler samples in each IR channel integration provided good CR rejection, while the six dithered exposures providing

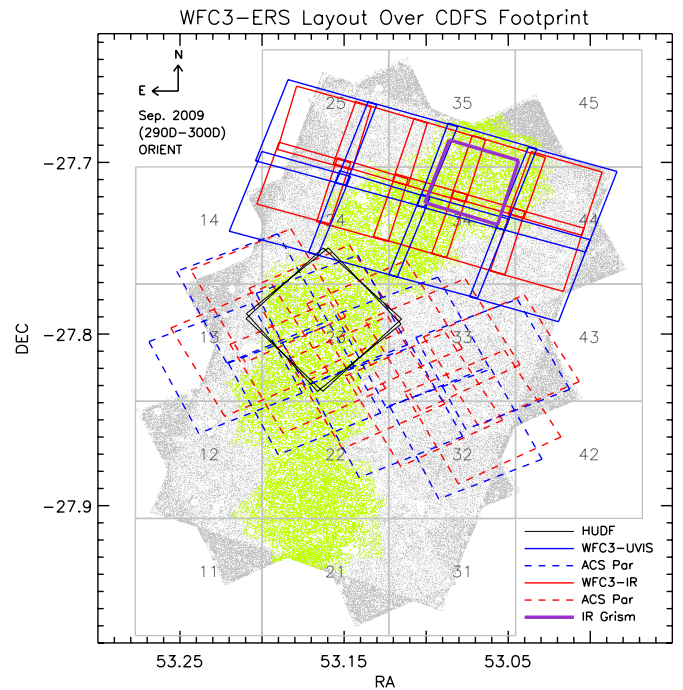


Figure 3. Layout of the GOODS-South field and its WFC3 ERS visits footprint. The light-gray area indicates the part covered by GOODS v2.0 data, and the numbered gray tiles are those of the GOODS-South survey. The green tiles indicate the GOODS-South area with ACS G800L grism data from the PEARS survey. The 4×2 ERS UVIS mosaic is superposed in blue, and the 5×2 ERS IR mosaic is superposed in red. The UVIS fields are numbered from left to right, with UVIS fields 1–4 in the top row and UVIS fields 5–8 in the bottom row. The IR fields are numbered from left to right, with IR fields 1–5 in the top row and UVIS fields 6–10 in the bottom row. The dashed blue and red boxes indicate the location of the ACS parallels to the ERS WFC3 images (Finkelstein et al. 2011). The ERS IR G102 and G141 grism field is shown by the purple box (see Figures 15(a)–(d)) and overlaps with the northern most of the PEARS ACS G800L grism fields in the GOODS-South region. The black boxes show the ACS Hubble Ultra Deep Field pointings in the GOODS-South field. The ERS program was designed to image the Northern $\sim 30\%$ of the GOODS-South field in six new WFC3 filters: F225W, F275W, and F336W in the UVIS channel, and F098M, F125W, and F160W in its IR channel. Further details are given in Tables 1 and 2. The exact pointings coordinates and observing parameters for all pointings in *HST* ERS program 11359 can be obtained from www.stsci.edu/observing/phase2-public/11359.pro.

the capability to properly drizzle the IR images, and so more properly sample the IR PSF (see Section 4.3.3).

HST scheduling required that this ERS program be split into several visits. Simple raster patterns were used to fill out the WFC3 IR mosaic, and to improve sky background plus residual dark-current removal. Only mild constraints were applied to the original *HST* roll angle (ORIENT) to maximize overlap between the northern part of the GOODS-South field, and to allow *HST* scheduling in the permitted observing interval for the ERS (2009 mid-September–mid-October). The IR and UVIS images were constrained to have the *same* ORIENT, to ensure that a uniform WFC3 mosaic could be produced at all wavelengths. The slight misalignment of the Northern edge of the *existing* ACS GOODS-South mosaics and the *new* WFC3 ERS mosaics in Figure 3 was due to the fact that the *HST* ORIENT constraints had to be slightly changed in the late summer of 2009, since the ERS observations needed be postponed by several weeks due to a change in the *HST* scheduling constraints. Since finding good guide stars for all 19 ERS pointing was very hard, it was necessary to only slightly change the mosaic ORIENT angles

at that point, but not the actual image pointing coordinates. The ERS mosaics would have otherwise become unschedulable.

The area of overlap between the individual WFC ERS mosaic pointings is too small to identify transient objects (e.g., SNe and variable AGNs), since only about 1%–2% of all faint field objects show point-source variability (Cohen et al. 2006). However, it is useful in the subsequent analysis to verify the positions of objects, and so verify the instrument geometric distortion corrections (GDCs) used, as discussed in Section 4 and Appendix A.

4. WFC3 UVIS AND IR DATA PROCESSING

The WFC3 ERS data processing was carried out with the STScI pipeline *calwf3*. The WFC3 ERS data set also provided tests of the STSDAS pipeline under realistic conditions. This process was started well before the SM4 launch in the summer of 2008 with pre-flight WFC3 thermal vacuum calibration data, and continued through the late summer and fall of 2009, when the first ERS data arrived. The raw WFC3 data was made public immediately, and the “On-The-Fly” pipe-lined calibrated and MultiDrizzled WFC3 mosaics will be made public via MAST at STScI when the final flight calibrations—as detailed below—have been applied. The specific pipeline corrections that were applied to the WFC3 ERS images are detailed here. Unless otherwise noted below, the latest reference files from the WFC3 Calibration Web site were used in all cases and are available on the Web.²⁶

4.1. The Main WFC3 Pipeline Corrections

4.1.1. WFC3 UVIS

All raw WFC3 UVIS data were run through the standard STSDAS *calwf3* calibration program as follows.

1. The best WFC3 UVIS super bias that was available at the time of processing (090611120_bia.fits) was subtracted from all images. This is an on-orbit super bias created from 120 UVIS bias frames, each of which was unbinned, and used all four on-chip amplifiers²⁷. The measured on-orbit UVIS read-noise levels are $3.1 e^-$ in Amp A, $3.2 e^-$ in Amp B, $3.1 e^-$ in Amp C, and $3.2 e^-$ in Amp D, respectively, or on average about $3.15 e^-$ per pixel across the entire UVIS CCD array.
2. A null dark frame was applied, since the only available darks at the time were from the ground-based thermal vacuum testing in 2007–2008, and these were not found to reduce the noise in the output ERS frames. Hence, the subtraction of actual on-orbit two-dimensional dark frames was omitted until better, high signal-to-noise ratio (S/N) on-orbit dark frames have been accumulated in Cycle 17 and beyond. Instead, a *constant* dark level of $1.5 e^- \text{ pix}^{-1} \text{ hr}^{-1}$ was subtracted from all the images, as measured from the *average* dark-current level in the few on-orbit dark frames available thus far. This dark level is about $5 \times$ higher than the ground-based thermal vacuum tests had suggested, but still quite low enough to not add significant image noise in an average 1200 s UVIS exposure.
3. A bad pixel file (tb41828mi_bpx.fits) was created (by H. Bushouse) and updated over the one available in the “Office of Space Sciences Payload Data Processing Unified

System” or “OPUS” pipeline at the time, and applied to all the UVIS images.

4. All flat-fields came from the 2007–2008 WFC3 thermal vacuum ground tests and had high S/N. We used these flats, since the WFC3 data base is not yet large enough to make a reliable set of on-board sky superflats. (As in the case for the WFPC2 Medium-Deep Survey, this can and will be done during subsequent years of WFC3 usage.) These thermal vacuum flats left some large-scale gradients in the flat-fielded data, due to the illumination difference between the thermal vacuum optical stimulus and the real on-orbit WFC3 illumination by the zodiacal sky background. For each passband, the mean UV sky background was removed from the individual ERS images (as part of MultiDrizzle), and the resulting images were combined into a median image in each UV filter. The large-scale gradients from this illumination difference correspond to a level of about $\sim 5\%$ – 10% of the on-orbit zodiacal sky background and have very low spatial frequency. This situation will be remedied with on-orbit internal flats and sky flats, that will be accumulated during Cycle 17 and beyond. Since the UV sky background is very low to begin with ($\sim 25.5 \text{ mag arcsec}^{-2}$; see Table 2 and Windhorst et al. 2002), these residual 1%–2% sky gradients affect the object photometry only at the level of $AB \gtrsim 27$ – 28 mag , i.e., well below the UVIS catalog completeness limits discussed in Section 5.4. Also, the spatial scales of these gradients are much larger than ~ 100 pixels, and faint objects are small (see Section 5.5 and figures therein; see also Windhorst et al. 2008), so that these gradients do not affect the faint object finding procedure, catalog reliability and completeness significantly (see Sections 5.1–5.4).

We suspect, but have at this stage not been able to prove with the currently available data, that this remaining low-level sky gradient is of *multiplicative* and not of *additive* nature. Once we have been able to demonstrate this with a full suite of sky flats, we will reprocess all the UVIS data again, and remove these low-level gradients accordingly. For now, these gradients are not visible in the high quality, high contrast color reproductions of Figures 5(a) and (b). Hence, they do not significantly affect the subsequent object-finding and their surrounding sky-subtraction procedures, which assume linear remaining sky gradients. This is corroborated by the quality of the panchromatic object counts discussed below, and consistency with the counts from other authors in the flux range where these surveys overlap. In other words, any remaining low-level sky gradients do not significantly affect the UVIS object catalogs generated for the current science purposes to $AB \simeq 25.5$ – 26.0 mag .

We also checked for CCD window ghosts or filter ghosts next to the brightest stars. These are in general very faint, or of very low surface brightness (SB) and much larger than the galaxies we are studying here. Such window ghosts do not affect the WFC IR images. In the WFC 3UVIS images, they only amount to 0.4% of the stellar peak flux in the F225W filter, and are much dimmer in the redder UVIS filters (Wong et al. 2010). No obvious filter ghost-like objects were found by the SExtractor object finder (Bertin & Arnouts 1996) surrounding the bright stars in the ERS.

4.1.2. WFC3 IR

The reduction of the ERS WFC3 IR data largely followed the procedures as described in Yan et al. (2011b). We used the *calwf3* task included in the STSDAS package to process the raw

²⁶ www.stsci.edu/hst/observatory/cdbs/SIfileInfo/WFC3/refitablequeryindex

²⁷ www.stsci.edu/hst/wfc3/lbn_archive/2009_09_09_new_uvis_superbias

WFC3 IR images, using the latest reference files indicated by the relevant FITS header keywords. Additional corrections to the calibrated images were applied as follows.

1. We removed residual DC offsets between the four detector quadrants, which was caused by an error in the application of the quadrant-dependent gain values in *calwf3* and documented in the WFC3 STAN (2009 September issue²⁸; see also Wong et al. 2010). Specifically, multiplicative gain correction factors were applied to each image quadrant using $g = 1.004$ for Quadrant 1 (upper left), $g = 0.992$ for Quadrant 2 (lower left), $g = 1.017$ for Quadrant 3 (lower right), and $g = 0.987$ for Quadrant 4 (upper right quadrant). Note that this quadrant issue was fixed in *calwf3v1.8* and later.
2. For each passband, the mean near-IR sky background was removed from the individual ERS images, and the resulting images were combined into a median image in each near-IR filter.
3. A smooth background gradient still persisted in the median image. This gradient was fitted by a five-order Spline function, and was then subtracted from the individual near-IR images. This sky gradient is of order 1%–2% of the zodiacal sky background. Since the near-IR zodiacal sky background is about 22.61, 22.53, and 22.30 mag arcsec⁻² in Y_s , JH (see Table 2), respectively, these remaining WFC3 IR gradients do not affect the large-scale object finding and catalog generation at levels brighter than $AB \simeq 27.0$ mag.

We checked for persistence in the IR images left over from saturated objects in previous exposures. Since the WFC3 IR observations just before the WFC3 ERS IR observations did not contain many highly saturated bright stars, very few obvious persistence problems were found. Since the ERS filters were taken in the order F125, F160W, F098M, persistence would have been most obvious in the highest throughput F125W filter, leading possibly to objects with unusually high J -band fluxes compared to H - and Y_s band. Only very few such objects were found, and where persistence was suspected, they were removed from the SExtractor catalogs.

4.2. WFC3 Astrometry and MultiDrizzle Procedures

4.2.1. WFC3 UVIS Astrometry

The calibrated, flat-fielded WFC3 UVIS exposures were aligned to achieve astrometric registration with the existing GOODS ACS reference frame (Giavalisco et al. 2004; GOODS v2.0²⁹ from Grogin et al. 2009). To generate accurate SExtractor (Bertin & Arnouts 1996) object catalogs in the F225W, F275W, and F336W filters, the higher-S/N GOODS ACS B -band images were used as the detection image. This also provided an astrometric reference frame that was matched as closely as possible to the wavelengths of the UVIS filters used in these observations. Because the GOODS B -band images reach $AB \lesssim 27.9$ mag and so go much deeper than the ERS UVIS images, they help optimally locate the objects in the ERS UVIS mosaics (see Section 5.1).

The F225W and F275W ERS exposures taken separately in successive orbits (see Section 3) needed to be aligned with each other individually, in addition to their overall alignment

onto the GOODS reference frame. For each ERS filter, the relative alignment between exposures was achieved iteratively, starting with an initial partial run of MultiDrizzle (Koekemoer et al. 2002) to place each exposure onto a rectified pixel grid. These images were then cross-correlated with each other, after median filtering each UVIS exposure and subtracting this smooth exposure to reduce the impact of cosmic rays and to identify the brighter real objects. This ensured a *relative* alignment between the sequential orbital ERS exposures to the sub-pixel level, correcting for offsets that were introduced by the guide-star acquisitions and re-acquisitions at the start of each successive ERS orbit.

4.2.2. The WFC3 UVIS MultiDrizzle Procedure

These first-pass aligned images were then run through a full combination with MultiDrizzle (Koekemoer et al. 2002), which produced a mask of cosmic rays for each exposure, together with a cleaned image of the field. The cosmic ray mask was used to create a cleaner version of each exposure, by substituting pixels from the clean, combined image. These were then rerun through the cross-correlation routine to refine the relative shifts between the exposures, achieving an ultimate relative alignment between exposures with an accuracy of $\lesssim 2$ –5 mas. This process was limited primarily by the on-orbit cosmic ray density, and the available flux in the faint UV objects visible in each individual UVIS exposure. In the end, about 3 independent input pixels from four exposures contributed to *one* MultiDrizzle UVIS output pixel. Of these, typically $\lesssim 1\%$ –2% were rejected in the cosmic ray rejection, leaving on average three independent UVIS measurements contributing to one MultiDrizzle output pixel in both the F225W and F275W filters. In F336W, about 2.3 independent input pixels from the three F336W exposures contributed to one output pixel during the MultiDrizzle process.

After this relative alignment between exposures was successfully achieved, each set of exposures needed to be aligned to the *absolute* GOODS astrometric reference frame. This was achieved by generating catalogs from the cleaned, combined images for each of the three ERS UVIS filters F225W, F275W, and F336W, and matching them to the GOODS B -band catalog (Giavalisco et al. 2004; Grogin et al. 2009). This was done by solving for linear terms (shifts and rotations) using typically ~ 30 –50 objects matched in each pointing, depending on the UVIS filter used. This procedure successfully removed the mean shift *and* rotational offsets for each visit relative to the GOODS astrometric frame. MultiDrizzle also produced “weight” maps (Koekemoer et al. 2002), which are essential for the subsequent object detection (Section 5.1), and for the computation of the effective area, which is needed for the object counts (see the figures in Sections 6 and 7).

In order to perform matched aperture photometry (see Section 5.2), our approach was to create images at *all* wavelengths at the same pixel scale. Since the IR data was necessarily created at 0.090 per pixel (see Appendix A), we created UVIS mosaics at that same pixel size. This essentially “smoothed” over the remaining issue of the geometric distortion solution (see Appendix A), and created a sufficient data product for the purpose of producing matched aperture photometric catalogs, reliable total magnitudes in all 10 ERS filters, performing $z \simeq 1$ –3 dropout searches, and many other “total magnitude applications.” The performance of the panchromatic ERS images for photometric redshift estimates is described by Cohen et al. (2011). Further details on the remaining uncertainties from

²⁸ www.stsci.edu/hst/wfc3/documents/newsletters/STAN_09_01_2009

²⁹ http://archive.stsci.edu/pub/hlsp/goods/v2/h_goods_v2.0_rdm.html

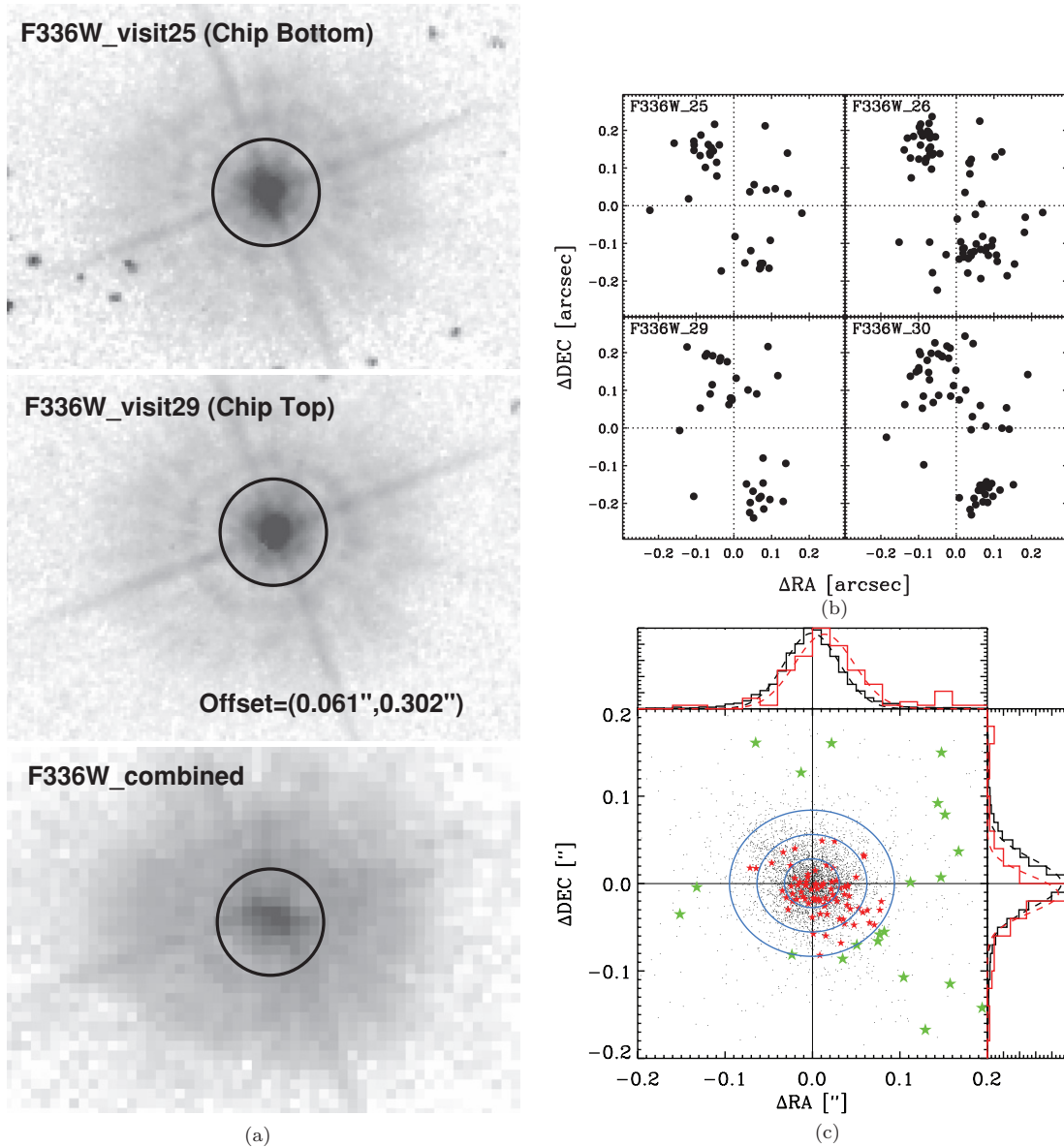


Figure 4. (a) ERS star imaged in the overlap region between UVIS visit 25 (upper panel) and visit 29 (middle panel) in the F336W filter. While the star is properly processed by MultiDrizzle in these *individual* visits (i.e., its images are round in the upper and middle panels), it is clearly displaced by (0.061'', 0.302'') in its WCS location between these two visits, as shown in the combined image (bottom panel). This is due to the wavelength-dependent geometric distortion correction (GDC). The GDC causes this star—and other objects in the mosaic *border* regions—to be elongated by approximately this amount when a MultiDrizzle is done of *all available* pointings, as can be seen in the bottom panel. A full wavelength-dependent GDC will make the images in the border regions round as well across the full MultiDrizzle mosaic. A proper measurement and continued monitoring of the wavelength-dependent GDC is scheduled for Cycle 18 and beyond. (b) Astrometric residuals for four of our ERS pointings in the F336W filter, defined as the differences between visits 25, 26, 29, or 30 and the image mosaic that was Multidrizzled using these four visits. Note that *all four* visits show similar bimodal residuals, suggesting that this is a systematic error. We suspect that this is due to the wavelength-dependent geometric distortion in the UV, since the only currently available distortion solution was measured in the F606W filter. Since two distinct groups of points occur in similar locations in all four panels, the MultiDrizzle images of objects seen in only one pointing—which includes 80%–90% of the total ERS area (see Figures 3 and 8(a))—are round at 0.090 pixel sampling. However, the images of the brighter objects in the overlap areas between mosaic pointings—10%–20% of the total area—are not always round, as can be seen in Figure 4(a). (We confirmed this by visual inspection of the F225W and F275W mosaics, where this trend is seen at lower S/N (see Appendix A), since faint stars are red (see Section 4.3.2).) (c) Measured residual astrometric offsets in (R.A., decl.) for all 4614 ERS objects in our WFC3 IR *H*-band object catalogs relative to our object catalogs based on the GOODS ACS/WFC v2.0 *z'*-band images. The 4511 ERS objects classified as galaxies are shown as small black dots, and the 103 ERS objects classified as stellar are shown as red or green asterisks. Histograms normalized to unity are also shown in each coordinate: black histograms indicate ERS galaxies and red histograms ERS stellar objects. Best-fit Gaussians are also shown for each of these histograms. Objects classified as ERS galaxies have a nearly Gaussian error distribution centered around $(\Delta R.A., \Delta \text{decl.}) = (0, 0)$, while objects classified as ERS stars have on average (red asterisks)—and in a significant number of individual cases (green asterisks)—significant evidence for proper motion at the $\gtrsim 3\sigma$ level. Further details are given in Sections 4.3.2 and 5.6.

(A color version of this figure is available in the online journal.)

the UV geometric distortion and its corrections are given in Appendix A and in Figures 4(a) and (b).

The current 0.090 per pixel UVIS image mosaic is referred to as “ERS version v0.7.” In the future, when the UV GDC

is well measured, and better on-orbit WFC3 flat fields or sky flats become available, we will make higher-resolution images (0.030 per pixel) for applications such as high-resolution faint-galaxy morphology, structure, half-light radii, and other

high-precision small-scale measurements of faint galaxies, and make these end-products available to the community.

4.2.3. IR Astrometry and MultiDrizzle Procedure

The WFC3 IR images processed as described in Section 3 were first corrected for the instrument geometric distortion and then projected to a pre-specified astrometric reference grid according to the World Coordinate System (WCS) information populated in the image headers. This was done by using the MultiDrizzle software (Koekemoer et al. 2002) distributed in the STSDAS.DITHER package. Similar to the processing of the UVIS images in Section 4.2.1, the GOODS version 2.0 ACS mosaics were used as the astrometric reference. The only difference is that the GOODS ACS mosaics were 3×3 rebinned for comparison with the ERS IR data, giving a spatial resolution of $0''.090$ per pixel for all ERS images.

As usual, the projected ERS IR images show non-negligible positional offsets, which is mainly caused by the intrinsic astrometric inaccuracies of the guide stars used in the different *HST* visits. Following Yan et al. (2011b), about 6–12 common objects were manually identified in each ERS IR input image and in the reference ACS z_{850} image. We subsequently solved for X – Y shift, rotation, and plate scale between the two. These transformations were then input to MultiDrizzle, and the drizzling process was rerun to put each input image onto the pre-specified grid. We set the drizzling scale (pixfrac) to 0.8, so that in the IR about 5 input pixels from four exposures, or 20 independent measurements contributed to 1 MultiDrizzle output pixel. Of these, typically $\lesssim 10\%$ or 2 pixels were rejected in the cosmic ray rejection, leaving on average 18 independent measurements contributing to one MultiDrizzle output pixel.

4.3. Resulting ERS Mosaics and their Properties

4.3.1. The Panchromatic 10-band ERS Mosaics

Figure 5(a) shows the panchromatic 10-band color image of the entire ERS mosaic in the GOODS-South field. All 10 ERS filters in Figures 5, 6, 13, and 14 are shown at the $0''.090$ pixel sampling discussed in Section 4. All RGB color images of the 10-band ERS data were made as follows. First, the mosaics in all 10 filters were registered to the common WCS of the ACS GOODS v2.0 reference frame to well within one pixel. Second, all images were rescaled to F_{ν} units of Jy per pixel using the AB zero points of Table 2. Next, the blue gun of the RGB images was assigned to a weighted version of the UVIS images in the F225W, F275W, and F336W filters and the ACS F435W filter. The green gun was assigned to a weighted version of the ACS F606W and F775W images, which had the highest S/N of all available images. The red gun was assigned to a weighted version of the ACS z -band (F850LP) and WFC3 IR F098M, F125W, and F160W images. All weighting was done with the typical image sky S/N, sometimes adjusted so as to not overemphasize the deepest multi-epoch GOODS v2.0 images in the V and i filters. This procedure thus also rebalanced the different sensitivities per unit time in these filters, as shown in Figures 1(a) and (b), and corrected for the fact that some filters have their central FWHM-range overlap somewhat in wavelength, so they are not completely independent (see Table 2). This is especially noticeable for the ACS z -band filter F850LP—which at the long wavelength side is cutoff by the sharp decline in the QE-curve of silicon—and the IR F098M filter, which does not have this problem at its blue side, but overlaps with F850LP for about 40% of its $\text{OTA} \times T \times$

QE integral, where OTA is the net OTA reflectivity, T in the product of the WFC3 optics reflectivities and filter + window transmissions, and QE is the detector Quantum Efficiency as a function of wavelength. (When the QE of the HgCdTe detectors produced by Teledyne increased from $\sim 10\%$ – 20% in 2001 to $\gtrsim 80\%$ after 2005, the F098M filter thus became almost a replacement of the ACS z band).

In Figures 5(a) and (b), we used a log(log) stretch to optimally display the enormous dynamic range of the full resolution ERS color TIFF images. Figure 5(a) only displays the overlap between the 4×2 ERS UVIS mosaics, the GOODS v2.0 ACS B V i z mosaics, and the 5×2 ERS IR mosaics. Each of the ERS mosaics are 8079×5540 pixels in total, but only about 6500×3000 pixels or $9''.75 \times 4''.5$ or 43.875 arcmin² is in common between the UVIS and IR mosaics and shown in Figures 5(a) and (b). The area of the individual UVIS mosaics used in each of the UV–optical galaxy counts of Section 7 is substantially larger than this, but the total usable area of the IR mosaics is comparable to the area shown in Figure 5(a).

Figure 5(b) (see Appendix B.1) shows a zoom of the 10-band ERS color image, illustrating the high resolution available over a factor of 10 in wavelength, the very large dynamic range in color, and the significant sensitivity of these few orbit panchromatic images. Further noteworthy objects in the images are discussed in Appendix B.1 below.

4.3.2. Astrometric Quality of the ERS Mosaics

To compare the astrometry of our WFC3 ERS catalogs to our catalogs derived from the GOODS ACS v2.0 images, we selected the WFC3 H band, because the geometrical distortion correction (GDC) was measured thus far in the F160W filter only (see Appendix A). Amongst the GOODS ACS v2.0 images, we select the z' -band filter as the closest in wavelength to compare the ERS F160W images to astrometrically, and because most faint ERS stars are expected to be red (see Section 5.5). The GDC of the ACS/WFC has been well measured and calibrated over time and as a function of wavelength (Maybhatte et al. 2010; Anderson 2002, 2003, 2007), and so is not a major source of uncertainty in this astrometric comparison. The exposure-time averaged effective epochs of the GOODS v2.0 ACS/WFC mosaics are: 2002.7796 in F435W, 2002.9755 in F606W, 2003.6083 in F775W and 2003.7634 in F850LP, respectively. Due to a continued GOODS high- z SN search that lasted from mid 2002 through early 2005, the spread on these numbers is about one year, yielding possibly somewhat elongated ACS images for very high proper motion stars in each of the GOODS v2.0 image stacks. The effective time-averaged epoch for the WFC UVIS ERS data is JD 2009.6918 in F225W, F275W, and F336W with a spread of 2 days, while for the WFC3 IR channel images the effective epoch is 2009.7370 in F098M, F125W, and F160W with a spread of about one week. For the WFC3 ERS images, image elongation for high proper motion stars is thus not a concern. The effective (WFC ERS–GOODS v2.0) epoch difference to be used for proper motions derived from this comparison is thus $(2009.7370 - 2003.7634) = 5.97 \pm 1$ years, where the dispersion is dominated by the GOODS ACS z' -band image spread of about one year.

Figure 4(c) shows the measured residual astrometric offsets in (R.A., decl.) for all 4614 ERS objects matched between our WFC3 H -band object catalog and our GOODS ACS/WFC v2.0 z' -band catalog, as well as their histograms in both coordinates for 4511 matched ERS objects classified as galaxies (black) and 103 ERS objects classified as stars (red). Best-fit Gaussians

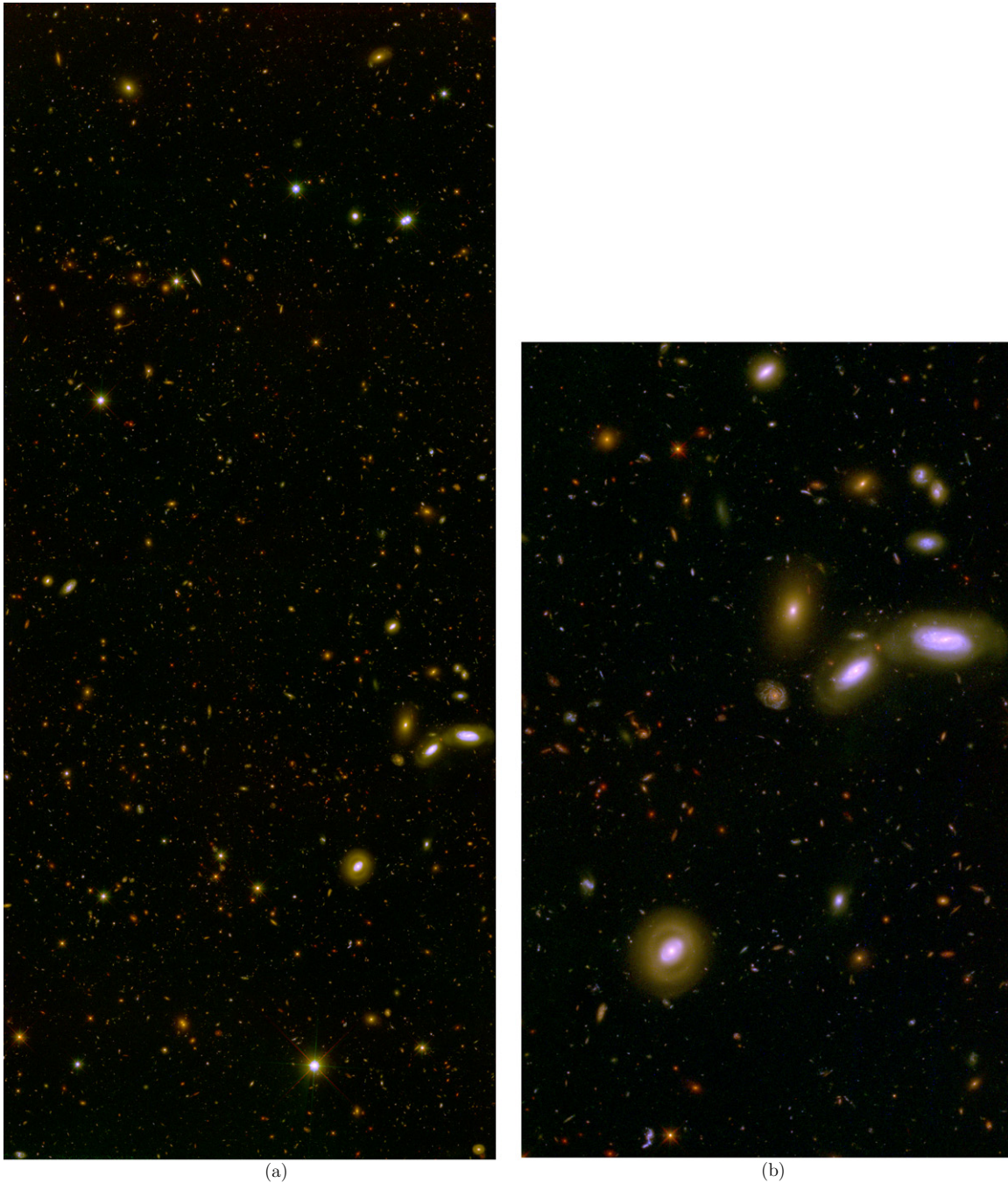


Figure 5. (a) Panchromatic 10-band color image of the entire ERS mosaic in the GOODS-South field. Shown are the common cross sections between the 4×2 ERS UVIS mosaics, the GOODS v2.0 ACS $BViZ$, and the 5×2 ERS IR mosaics. The total image shown is 6500×3000 pixels, or 9.75×4.5 . We used color weighting of the 10 ERS filters as described in the text, and log(log) stretch. (For best display, please zoom in on the full-resolution version of this image, which is available on http://www.asu.edu/clas/hst/www/wfc3ers/ERS2_loglog_levay.tif.) Note that in these color images the reddest objects are *not* necessarily at $z > 7$, due to the way the colors were combined. (b) Enlargement of the panchromatic 10-band ERS color image in the GOODS-South field (see Figure 5(a)). (For best display, please zoom in on the full-resolution version of this image, which is available on http://www.asu.edu/clas/hst/www/wfc3ers/ERS2_gxysv4ln.tif.)

are also shown for each of the histograms. As discussed in Section 4.2, the WCS coordinate system in the FITS headers of the WFC3 ERS images was by definition brought onto the well established GOODS ACS v2.0 WCS. This was done by applying WCS offsets averaged over *all* ERS objects to the WFC3 FITS headers. The histograms and curves in Figure 4(c) show that this could be done with an accuracy of 0.32 ± 0.46 (m.e.) mas in R.A., and 0.10 ± 0.41 (m.e.) mas in decl., respectively, i.e., in general to within 0.5 mas both randomly and systematically. While residual errors in the WFC3 GDC are

large (see Section 4.2 and Appendix A), for a large number of objects spread over all the ERS images these errors apparently average out well enough to establish the overall WCS coordinate system of both the ERS UVIS and IR mosaics onto the GOODS v2.0 ACS/WFC mosaics to within 0.4–0.5 mas on average.

For the 4511 ERS galaxies *alone*, Figure 4(c) shows that the residual WFC3 offsets compared to GOODS ACS v2.0 are $\Delta R.A. = -0.64 \pm 0.47$ (m.e.) mas and $\Delta decl. = +0.38 \pm 0.42$ (m.e.) mas, or at the 1.4 and 0.9σ level in R.A. and decl., respectively. For the galaxies, these ERS offsets are indeed

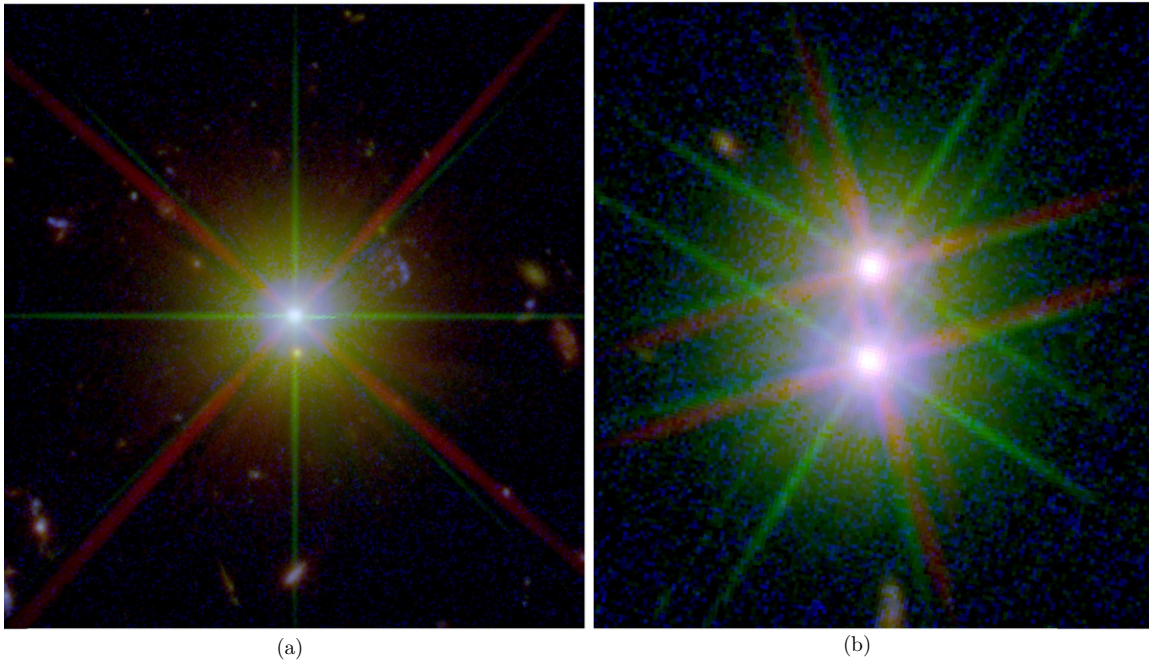


Figure 6. (a) $\log(\log)$ color reproduction of a bright but unsaturated star image in the 10-band ERS color images in the GOODS-South field, using the same color balance prescription as in Figures 5(a) and (b). (b) Same for a “double” star. These images give a qualitative impression of the significant dynamic range in both intensity and wavelength that is present in these panchromatic ERS images. (c) $\log(\log)$ color reproduction of the 20 ERS stars with the highest ($\gtrsim 3\sigma$) proper motion, as discussed in Section 4.3.2 and Figure 4(c). Each image is 85×85 pixels or $7''.65 \times 7''.65$ on the side. The images used a similar color balance as in Figures 5(a) and (b), except that only the 2009 WFC3 UVIS filters F225W, F275W, and F336 are now in the blue gun, all the 2003 ACS *BVIz* filters F438W, F606W, F775W, and F850LP are in the green gun, and the 2009 WFC3 IR filters F098M, F125W, and F160W are in the red gun. The RGB colors were further adjusted such that the proper motion between the Green 2003 ACS colors and the Blue+Red (or violet) 2009 WFC3 colors were maximally contrasted. In many cases, the proper motion is visible as an offset between the centroids of the Green and the Red+Blue images. For details, see the text.

statistically insignificant, although they are not exactly equal to zero, because the matching onto the ACS WCS was done including the ERS stars as well—*before* it was known what the optimal star–galaxy separation method would be. (Because the residual offsets for *all* ERS galaxies alone are within the 0.4–0.5 mas errors quoted above, no second iteration was done in bringing the WFC3 WCS system on top of the GOODS ACS v2.0 WCS system.)

In total, 21 out of the 103 ERS stellar candidates show proper motion at the $\geq 3\sigma$ level in R.A. or decl., respectively, as shown by the green asterisks in Figure 4(c). In total, 37 out of the 103 ERS stellar candidates show proper motion at the $\geq 2\sigma$ level, also shown in Figure 4(c). Only about five stars are expected at $\geq 2\sigma$ for a random Gaussian distribution, and so the stellar (Δ R.A., Δ decl.) offsets have a non-Gaussian distribution, as shown by the histograms in Figure 4(c). Hence, proper motion allows us to confirm statistically about 32 out of the 103 stellar candidates in the ERS. As a consequence, ERS proper motions *alone* cannot prove that *all* our ERS objects classified as stellar are in fact Galactic stars. For this reason, we will also consider object colors in Section 5.5 as confirmation of the stellar classifications.

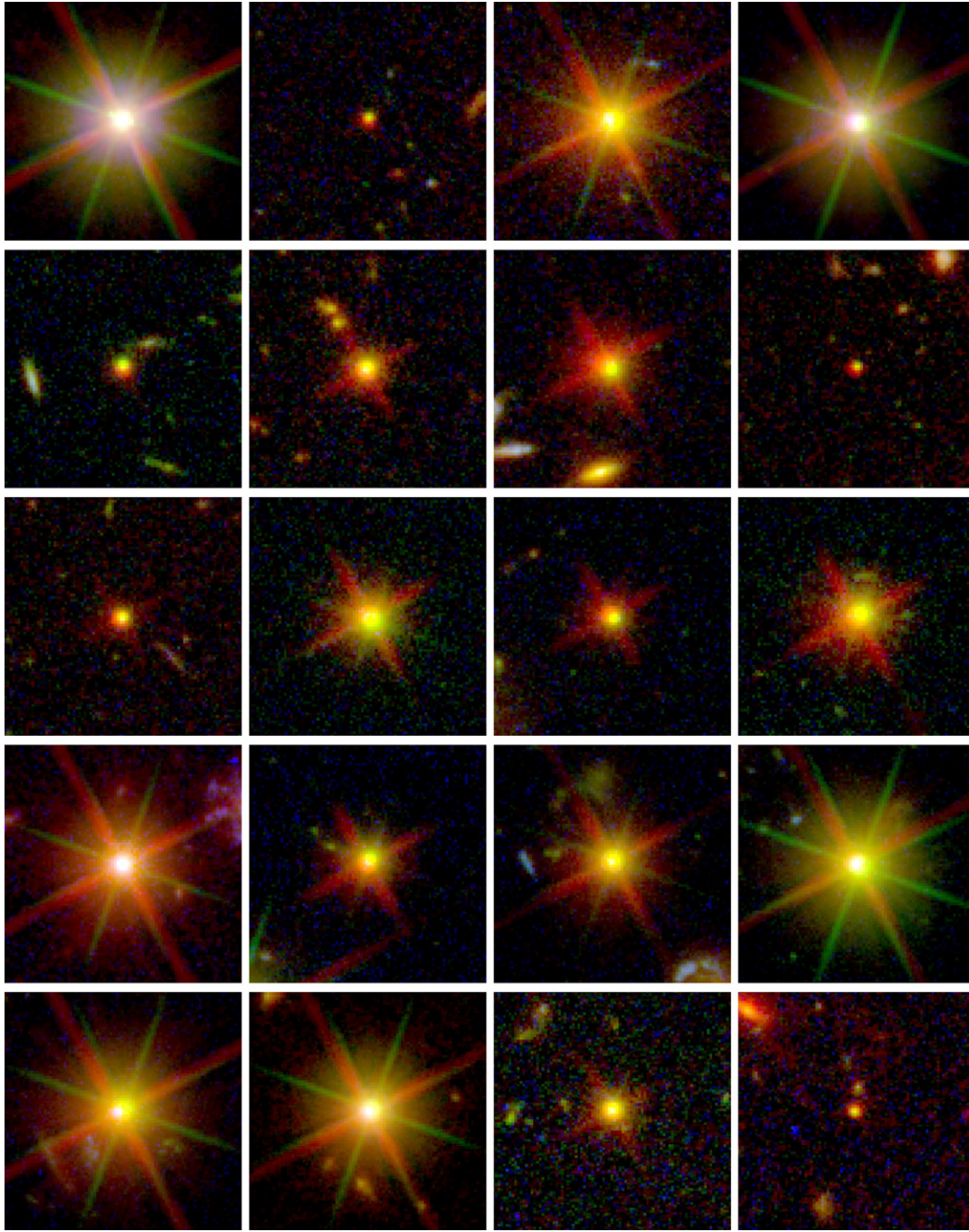
Statistically, proper motions do cause significant offsets in the average (Δ R.A., Δ decl.) distribution of the 103 ERS objects classified as stars (Figure 4(c)). For these stellar candidates, we find on average that Δ R.A. = 13.71 ± 3.34 (m.e.) mas, or 2.30 ± 0.56 mas yr $^{-1}$, and Δ decl. = -12.04 ± 2.09 (m.e.) mas, or 2.02 ± 0.35 mas yr $^{-1}$. These constitute 4.1σ and 5.8σ detections of the statistical proper motion of all 103 ERS stellar candidates. The KS probability that the stellar Δ R.A. values are drawn from same distribution as the ERS galaxy population is 9.8×10^{-5} , while for the stellar Δ decl. values this probability

is 11×10^{-5} . Hence, *average* stellar proper motion is detected at high significance level for the sample of 103 ERS stellar candidates. This is a significant result, since the star–galaxy separation of Section 5.5 was done completely independent of any proper motion information. A further discussion of this result is given in Sections 5.6 and 6.

Figure 6(c) shows a $\log(\log)$ color reproduction of the 20 ERS stars with the highest ($\gtrsim 3\sigma$) proper motion (green symbols in Figure 4(c)). The images used a similar color balance as in Figures 5(a) and (b), except that only the 2009 WFC3 UVIS filters are shown in the blue gun, *all* the 2003 ACS *BVIz* filters were used in the green gun, and all the 2009 WFC3 IR filters in the red gun. The proper motion of these stars is best visible as significant centroid-displacements between the Green 2003 ACS colors and the Blue+Red (or violet) 2009 WFC3 colors (one has to magnify the PDF figure to best see the significant central green-to-white-to-orange displacement).

4.3.3. The Panchromatic ERS PSFs

Figure 6(a) shows a full color reproduction of a stellar image in the 10-band ERS color images in the GOODS-South field, and Figure 6(b) shows a “double” star. These images give a qualitative impression of the significant dynamic range in both intensity and wavelength that is present in the ERS images. Figure 7(a) shows images in all 10 ERS filters of an isolated bright star that was unsaturated in all filters, and Figure 7(b) shows its 10-band stellar light profiles. Table 2 lists the stellar PSF FWHM values in the 10 ERS bands. These include the contribution from the OTA and its wavefront errors and the specific instrument pixel sampling.



(c)

Figure 6. (Continued)

Table 2 and Figure 7(b) show the progression of the *HST* PSF (λ/D) with wavelength in the 10 ERS filters. Table 2 implies that the larger pixel values used in the multidrizzling of Section 4.2.2 indeed add to the effective PSF diameter. Table 2 also shows that that *HST* is diffraction limited in *V* band and longward, while shortward of *V* band, the PSF FWHM starts to increase again due to mirror micro-roughness in the ultraviolet. At wavelengths shorter than the *V* band, *HST* is no longer diffraction limited, resulting in wider image wings, and a somewhat larger fraction of the stellar flux visible outside the PSF core. The “red halo” at $\lambda \gtrsim 0.8 \mu\text{m}$ is due to noticeable Airy rings in the stellar images in the WFC3 IR channel, and the well known red halo in the ACS *z* band (Maybhate et al. 2010) has an additional component

from light scattered off the CCD substrate. Details of the on-orbit characterization of the WFC3 UVIS and IR PSFs are given by Hartig (2009a, 2009b).

4.3.4. The 10-band ERS Area and Depth

Table 1 summarizes the exposure times and the actual achieved depth in each of the observed ERS filters, while Table 2 also lists the effective area covered in each filter mosaic at the quoted depth.

The histograms of Figures 8(a)–(c) give the cumulative distribution of the maximum pixel area that possesses a specified fraction of total orbital exposure time. These effective areas

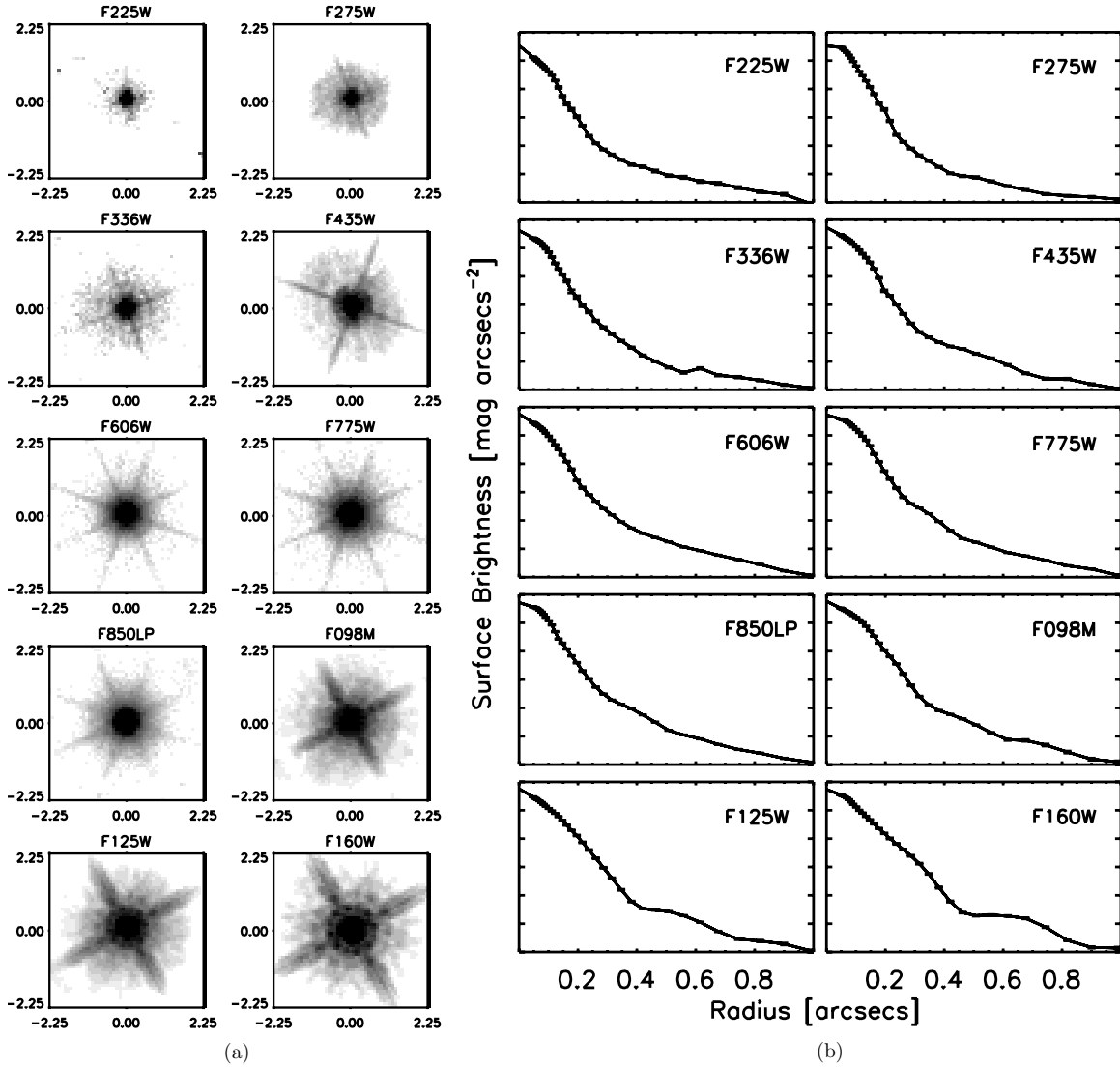


Figure 7. (a) Stellar images, and (b) Stellar light profiles in the individual 10-band images. Note the progression of the PSF size with wavelength, as discussed in Section 4.3.2.

must be quantified in order to properly do the object counts in Sections 6 and 7. After Multidrizzling the ERS mosaics in the UV and IR, these effective areas were computed from the weight maps, which include the total exposure time, and the effects from CR rejection, dithering, and drizzling. Figure 8(a) shows that about 50 arcmin² of the UV mosaics has $\sim 80\%$ of the UVIS exposure time, or $\sim 90\%$ of the intended UV sensitivity. For reference, one 0''.090 pixel could be composed of 5.2 native WFC3 UVIS pixels times the number of exposures on that portion of sky. Due to overlapping dithers (see Figure 3), some pixels have more than the total orbital exposure time contributing to their flux measurement. The histograms of Figure 8(b) give the same information as Figure 8(a), but for the six GOODS v2.0 mosaic tiles in *BVi*z that overlap with the ERS. Figure 8(c) gives the same information as Figure 8(a), but for the ERS mosaics in the IR. About 40 arcmin² has $\sim 80\%$ of the exposure time in the ERS IR mosaics, or $\sim 90\%$ of the intended IR sensitivity. The overall WFC3 UVIS–IR sensitivity is 9%–18% better than predicted from the ground-based thermal vacuum tests (see Section 2.4 and Figure 2), and so in essence 100% of the intended ERS exposure time was achieved over the 50 arcmin² UVIS images and the 40 arcmin² IR images.

5. CATALOG GENERATION FROM THE 10-BAND ERS MOSAICS

5.1. Object Finding and Detection

All initial catalogs were generated using SExtractor version 2.5.0 (Bertin & Arnouts 1996). In general, these catalogs were generated SExtractor’s *single image mode* for each ERS filter separately, so that the object finding could be done using the *total* object flux from each ERS filter independently, as is required when determining the star counts (Section 6) and the galaxy counts (Section 7). SExtractor was *only* used in its *dual image mode* to generate the *additional* catalogs that were used exclusively to make the color–color diagrams in Section 5.6 to confirm our star–galaxy separation procedure, using the *H* band as the detection image. As stated in Section 4.2.1, the ACS *B*-band image was used as the detection image to get an optimal object definition in the UVIS filters for reasons explained in detail here.

It was necessary to change the parameters in SExtractor to handle the UVIS images slightly differently than the ACS/WFC and WFC3/IR ones. This is due to several factors, both cosmetic and physical. The major difference is that galaxies